RESEARCH ARTICLE

National Science Review
9: nwab122, 2022
https://doi.org/10.1093/nsr/nwab122
Advance access publication 5 July 2021

PHYSICS

Room-temperature coherent manipulation of single-spin qubits in silicon carbide with a high readout contrast

Qiang Li[1,2,†], Jun-Feng Wang[1,2,†], Fei-Fei Yan[1,2], Ji-Yang Zhou[1,2], Han-Feng Wang[1,2], He Liu[1,2], Li-Ping Guo[3], Xiong Zhou[3], Adam Gali[4,5,*], Zheng-Hao Liu[1,2], Zu-Qing Wang[1,2], Kai Sun[1,2], Guo-Ping Guo[1,2], Jian-Shun Tang[1,2], Hao Li[6], Li-Xing You[6], Jin-Shi Xu[1,2,*], Chuan-Feng Li[1,2,*] and Guang-Can Guo[1,2]

[1]CAS Key Laboratory of Quantum Information, University of Science and Technology of China, Hefei 230026, China; [2]CAS Center for Excellence in Quantum Information and Quantum Physics, University of Science and Technology of China, Hefei 230026, China; [3]Key Laboratory of Artificial Micro- and Nano-structures of Ministry of Education and School of Physics and Technology, Wuhan University, Wuhan 430072, China; [4]Department of Atomic Physics, Budapest University of Technology and Economics, Budafoki út. 8, H-1111, Hungary; [5]Wigner Research Centre for Physics, Budapest 1121, Hungary and [6]State Key Laboratory of Functional Materials for Informatics, Shanghai Institute of Microsystem and Information Technology, Chinese Academy of Sciences (CAS), Shanghai 200050, China

*Corresponding authors. E-mails: gali.adam@wigner.hu; jsxu@ustc.edu.cn; cfli@ustc.edu.cn
†Equally contributed to this work.

Received 14 January 2021; **Revised** 21 June 2021; **Accepted** 21 June 2021

ABSTRACT

Spin defects in silicon carbide (SiC) with mature wafer-scale fabrication and micro/nano-processing technologies have recently drawn considerable attention. Although room-temperature single-spin manipulation of colour centres in SiC has been demonstrated, the typically detected contrast is less than 2%, and the photon count rate is also low. Here, we present the coherent manipulation of single divacancy spins in 4H-SiC with a high readout contrast (−30%) and a high photon count rate (150 kilo counts per second) under ambient conditions, which are competitive with the nitrogen-vacancy centres in diamond. Coupling between a single defect spin and a nearby nuclear spin is also observed. We further provide a theoretical explanation for the high readout contrast by analysing the defect levels and decay paths. Since the high readout contrast is of utmost importance in many applications of quantum technologies, this work might open a new territory for SiC-based quantum devices with many advanced properties of the host material.

Keywords: silicon carbide, single divacancy defects, spin coherent control, high readout contrast, bright photon emission

INTRODUCTION

Colour centres in silicon carbide (SiC) have recently attracted broad interest as electrically driven, highly bright single-photon sources and defect spins with long coherence time [1–12]. The most widely studied spin defects in SiC are divacancies (missing a silicon atom and an adjacent carbon atom, $V_{Si}V_C$) [12–15], silicon vacancies (missing a silicon atom, V_{Si}) [11,16–19] and nitrogen-vacancy centres (consisting of a nitrogen impurity substituting a carbon atom and a silicon vacancy adjacent to it, N_CV_{Si}) [20–23], the spin states of which can be optically polarized and readout. Although hundreds of SiC polytypes exist, many works focus on a specific polytype, namely the 4H polytype (4H-SiC), due to its high crystal quality. On the other hand, the $V_{Si}V_C$ defects in SiC are near-infrared photoluminescence (PL) emissions and have versatile applications, including quantum information processing [24] and multifunctional sensing, such as magnetic fields [25], electric fields [26], strain [27,28] and temperature [29,30]. Moreover, these defect spins can be flexibly controlled by microwaves [9,10], electronics [15,31] and acoustics [32], which have garnered great interest.

Depending on the location of the vacancies (hexagonal (*h*) and quasi-cubic (*k*)), four identified types of $V_{Si}V_C$ defects exist in 4H-SiC, namely, *hh* (PL1), *kk* (PL2), *hk* (PL3) and *kh* (PL4) defects [14,25]. In addition to the four known types of $V_{Si}V_C$ defects, there are also the PL5, PL6 and PL7 defects [14,25] that have recently been assigned to divacancy configurations inside stacking faults, which act as local quantum wells in 4H-SiC and make PL5–PL7 colour centres robust against photo-ionisation [33]. Thus, we use $V_{Si}V_C$ to refer to the PL1–PL7 defects. Although room-temperature single-spin manipulation of colour centres in SiC has been previously demonstrated [11,34], the typical detected contrast is less than 2%, and the

photon count rate is also low, which limits their applications.

In this work, we prepare arrays of single $V_{Si}V_C$ defects in 4H-SiC through carbon ion (C^+) implantation and annealing. We then investigate the spin and optical properties of single $V_{Si}V_C$ defects at room temperature. Surprisingly, for single PL6 defects, the single-photon saturated count rate is up to 150 kcps (kilo counts per second), which is almost 5 times and 15 times higher than that of single PL1–PL4 divacancies [9,10] and single V_{Si} in bulk 4H-SiC [11,35], respectively. Moreover, the contrasts of the continuous-wave- (CW) optically detected magnetic resonance (ODMR) spectrum and the Rabi oscillation are approximately −23% and −30%, respectively (the negative sign is consistent with the pulsed ODMR contrast discussed below) at room temperature. These outstanding properties are comparable with those of the nitrogen-vacancy (NV) centres in diamond [36,37]. The coupling between a single PL6 defect spin and a nearby nuclear spin (^{29}Si) is further detected. We also provide a theoretical explanation for the high readout contrast by analysing the defect levels and decay paths in the defects.

To our knowledge, this is the second solid-state defect qubit that exhibits such unique properties in terms of a high readout contrast together with a high photon count rate at room temperature, but in a technologically mature material with a wavelength region that is favourable for biological quantum sensing and quantum communication applications. Efficiently generated single divacancy defects in SiC with high-quality room-temperature optical and spin properties would be suitable for nanoscale sensing and helpful for constructing hybrid quantum devices under ambient conditions.

EXPERIMENTAL RESULTS

The implanted sample was annealed at 900 °C for 30 minutes to prepare the single defects (the low-temperature photoluminescence spectra can be found in Section 1 of the online supplementary material). The detailed process of sample preparation can be found in the Methods section. In the experiment, a 920-nm CW laser within the range of optimal excitation wavelengths [38] was used to excite the colour centres. Figure 1(a) shows a representative confocal fluorescence image within an area of $32 \times 32\ \mu m^2$ using home-built confocal microscopy with an oil objective of 1.3 NA (see the Methods section for more details). The pumping power is set to 1 mW. In the image, some of the bright points are still shown to be single defects. For example, the defect denoted by the orange circle is a single PL6 defect, which will be investigated in detail later.

We characterize the optical properties of the single PL6 defect, denoted by the orange circle in Fig. 1(a) at room temperature. The second-order intensity correlation function was measured at different excitation laser powers (Fig. 1(b)). The obvious photon-bunching phenomenon in the Hanbury-Brown and Twiss (HBT) measurement under the situation of a high exciting laser power implies the existence of a metastable state [5]. The background-corrected experimental data are fitted by the equation $g^{(2)}(t) = 1 - (1 + a)e^{-|t|/\tau_1} + de^{-|t|/\tau_2}$, where a, d, τ_1 and τ_2 are the fitting parameters [39,40] (the values of $g^{(2)}(t)$ deduced from the raw data are shown in Section 2 of the online supplementary material for comparison). The values of $g^{(2)}(0)$ at different exciting laser powers are all less than 0.5, indicating a single-photon emitter. We also measured the time traces of the fluorescence intensity of a single PL6 defect with a sampling time of 0.1 s at exciting laser powers of 0.2 mW (black), 1 mW (orange), 3 mW (blue) and 9 mW (green), as shown in Fig. 1(c). The experimental results indicate that the fluorescence emission of the single PL6 defect at different exciting laser powers is photostable. We further measured its saturation behaviour (Fig. 1(d)). The background-corrected experimental data (purple rhombuses) are fitted with the function $I(P) = I_s \cdot P/(P + P_s)$ (solid red line). The saturated exciting power P_s is 0.75 ± 0.01 mW, and the saturated PL intensity I_s is 150.8 ± 0.7 kcps. We also measured the saturated PL intensity of several other randomly selected single PL6 defects. The saturated PL intensity of these single PL6 defects ranges from 138.9 kcps to 172.4 kcps, with an average value of 155.9 kcps (see Section 2 of the online supplementary material). We observed spin-selective optical lifetimes at 13.4 ± 0.3 ns and 8.9 ± 0.1 ns at room temperature (see Section 3 of the online supplementary material), which implies a sizable ODMR contrast for single PL6 defects at ambient conditions (see the Theoretical Analysis section below).

We then use a common ODMR method (see the Methods for more details) to characterize the spin properties of the single PL6 defect at room temperature, which is widely used for NV centres in diamond or divacancies in SiC [14,41]. The CW-ODMR spectrum in the zero magnetic field excited with a 50-μW laser is shown in Fig. 2(a). Because of the spin polarization-dependent emission, a change is inevitable in the PL readout (ΔPL) with and without the resonant microwave (MW). The oscillation frequency between $m_s = 0$ and $m_s = \pm 1$ is 1.3514 GHz [14,25], and the ODMR contrast is deduced to be −23% (see Section 4 of the online

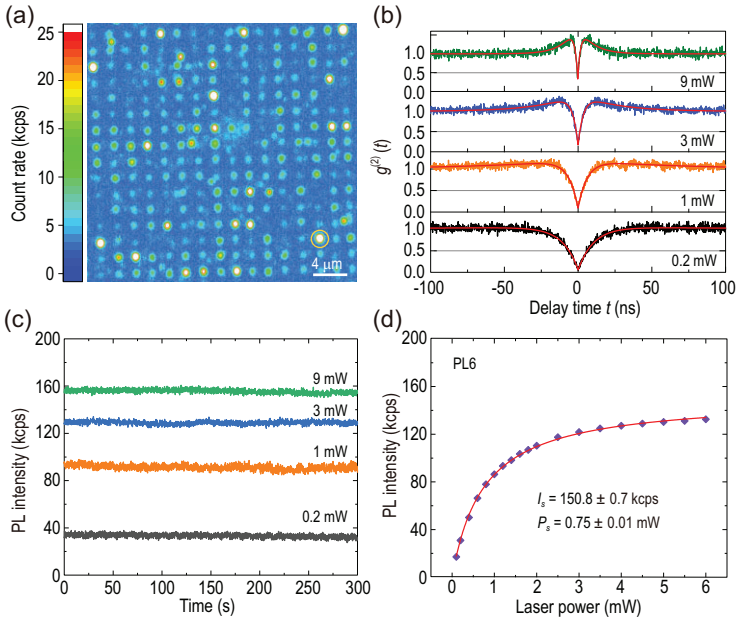

Figure 1. Characterization of the single $V_{Si}V_C$ defect arrays generated by 30 keV carbon ion implantation. (a) Representative confocal fluorescence image (32 × 32 μm^2) of the implanted sample. The white scale bar is 4 μm. The bright point in the orange circle represents the single PL6 defect used in (b)–(d). (b) Second-order intensity correlation function of $g^{(2)}(t)$ for exciting laser powers of 0.2 mW (black), 1 mW (orange), 3 mW (blue) and 9 mW (green). The red lines are the corresponding fittings. (c) Photostability at exciting laser powers of 0.2 mW (black), 1 mW (orange), 3 mW (blue) and 9 mW (green). The sampling time is 0.1 s, and the duration time is 300 s. (d) Saturation behaviour. The purple rhombuses are the background-corrected experimental data and the red solid line is the fitting with a function of $I(P) = I_s \cdot P/(P + P_s)$, where P and $I(P)$ are the exciting laser power and the corresponding count rate, respectively, with I_s and P_s being the saturated count rate and saturated exciting power, respectively.

supplementary material for details on the optimization of ODMR contrast). We further demonstrate the ODMR signals as a function of the magnetic field, which is arranged to be parallel to the crystal c axis (Fig. 2(b)). The slope of splitting between $m_s = \pm 1$ and $m_s = 0$ is ± 2.80 MHz/G due to the Zeeman effect. The Rabi oscillation of the single spin between the $m_s = 0$ and $m_s = -1$ states in a magnetic field of 26.4 G is shown in Fig. 2(c), where the readout contrast is deduced to be approximately −30%. We also measure the Rabi oscillation contrast of several other single PL6 defects. The Rabi oscillation contrast ranges from −23.0% to −31.6% with an average value of −26.4% (see Section 2 of the online supplementary material). We then characterize the coherence properties of the single PL6 defect spin at room temperature (see the Methods section). The Ramsey oscillation is measured in a magnetic field of 330 G, which is shown in Fig. 2(d). The experimental data (blue dots) are fitted using a two-cosine exponential decay function (red line), from which the inhomogeneous spin-dephasing time T_2^* is deduced to be 463 ± 35 ns. The Hahn echo is also measured in a magnetic field of 330 G (Fig. 2(e)), from which the homogeneous spin coherence time T_2 is deduced to be 23.2 ± 2.5 μs. The coherence time can be readily elongated via dynamical decoupling techniques [42]. In this work, Carr-Purcell-Meiboom-Gill (CPMG) decoupling sequences [43] are used to prolong the spin coherence time T_2 of single PL6 defects. Taking advantage of the CPMG-2 sequences, the coherence time T_2 of a selected single PL6 defect spin is extended from 30.2 ± 5.5 μs to 41.1 ± 3.5 μs. As the number of π pulses in the CPMG sequence increases, the coherence time of the electronic spin is extended (see Section 5 of the online supplementary material for more details). The longitudinal coherence time T_1 is further measured to be 149.1 ± 12.4 μs in a magnetic field of 220 G, which is shown in Fig. 2(f) (see Section 6 of the online supplementary material for the measuring method). The spin coherence time T_2 of the single PL6 defect is shorter than that in the as-grown high-purity semi-insulating (HPSI) 4H-SiC [14,30], presumably because of the high nitrogen doping level in the used samples (5 × 10^{15} cm^{-3}) and material damage from the ion implantations [25]. The coherence time T_2 can be dramatically improved by using SiC samples with lower nitrogen concentrations and isotopic purification [44,45], as well as by optimizing the conditions of implantation and annealing, similar to the strategies usually adopted for NV centres in diamond [46,47].

In this work, we determined the single emitter by measuring the second-order intensity correlation function ($g^{(2)}(t)$) for the isolated bright spots generated by C^+ ion implantation and annealing. The values of $g^{(2)}(0)$ deduced from the raw data and the background-corrected results are both far less than 0.5, indicating a single defect (see the online supplementary material for more detailed information). In addition, we identified the types of single defects by measuring the ODMR spectra at room temperature or detecting the corresponding fluorescence spectra at a cryogenic temperature of 8 K (see Section 1 of the online supplementary material). Figure 3 demonstrates the spin properties of a single PL5 defect at room temperature, and Fig. 3(a) shows the zero-field CW-ODMR spectrum of a single PL5 defect with 50-μW laser pumping. The oscillation frequencies are 1.3757 GHz and 1.3437 GHz, respectively [14,25]. It is worth noting that the CW-ODMR contrast of the single PL5 defect spin can approach −18%. We focus on the right branch to investigate coherent manipulation. The Rabi oscillation of the single PL5 defect spin with a zero magnetic field is demonstrated in Fig. 3(b), where the readout contrast of the Rabi oscillation is approximately −25%. We also measured the Rabi

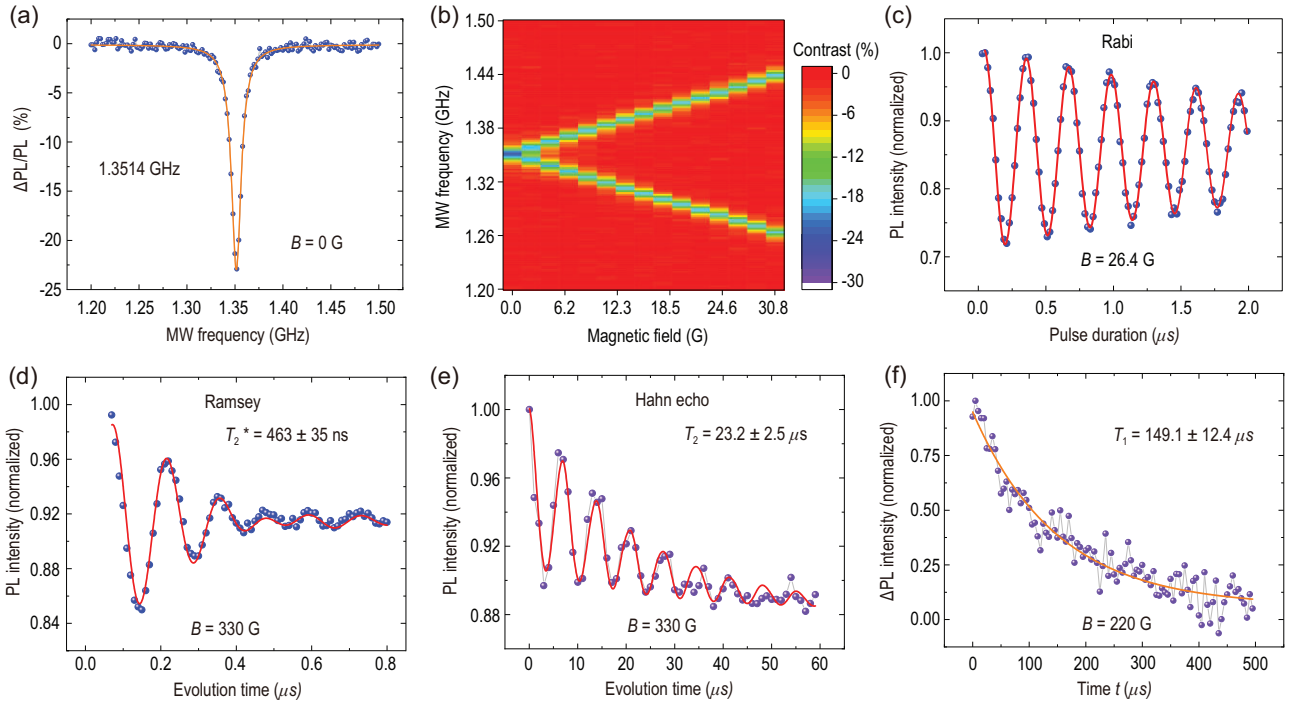

Figure 2. Spin properties of a single PL6 defect at room temperature. The magnetic field is arranged to be parallel to the crystal *c* axis. (a) CW-ODMR spectra in the zero magnetic field. The blue dots are the experimental raw data, and the orange line is the corresponding Lorentzian fitting centred at 1.3514 GHz. (b) The CW-ODMR spectra as a function of the magnetic field intensities. (c) Rabi oscillation measured in a magnetic field of 26.4 G. (d) Ramsey oscillation measured in a magnetic field of 330 G. From the fitting, the inhomogeneous spin-dephasing time T_2^* is deduced to be 463 ± 35 ns. (e) Hahn echo coherence time measured in a magnetic field of 330 G. From the fitting, the homogeneous spin coherence time T_2 is 23.2 ± 2.5 μs. (f) A representative measurement of T_1 with a magnetic field of 220 G. The purple dots are the experimental data, which are fitted by a single-exponential decay function.

oscillation of several other single PL5 defects. The Rabi oscillation contrast ranges from −23.6% to −28.5%, with an average value of −26% (see Section 7 of the online supplementary material). The Ramsey and Hahn echo measurements of the single PL5 defect spin are demonstrated in Fig. 3(c) and (d), respectively. From the fitting, the inhomogeneous spin-dephasing time T_2^* and the Hahn echo coherence time T_2 of the single PL5 defect without a magnetic field at room temperature are deduced to be 1.66 ± 0.19 μs and 24.0 ± 2.4 μs, respectively. More optical and spin properties of the single PL5 defect can be found in Section 7 of the online supplementary material.

We also investigated the spin properties of single PL1 and PL7 defects at room temperature (see Section 8 of the online supplementary material). The contrasts of Rabi oscillation of single PL1 and PL7 are approximately −6.6% and −10%, respectively, which are both lower than those of PL5 and PL6. The properties of PL1-7 are summarized in Table S1 of the online supplementary material. We further measured the generation ratio of single PL5, PL6 and PL7 defects in a 10 × 10 array of implanted sites, which are obtained to be 7%, 1% and 6%, respectively (see Section 9 of the online supplementary material).

For the SiC sample with natural abundance, there are 4.7% ^{29}Si with nuclear spin $I_{\rm Si} = 1/2$ and 1.1% ^{13}C with nuclear spin $I_{\rm C} = 1/2$. In the implanted sample, it is easy to find a single defect spin strongly coupled with a nearby nuclear spin, even at room temperature. The ODMR spectra of a single PL6 defect spin coupled with a nearby ^{29}Si nuclear spin (Si_{IIb} lattice site) [24,48] are measured in a *c*-axis magnetic field of 28.6 G, which is shown in Fig. 4(a). The splitting of two sets of dips results from the Zeeman effect, and the splitting of adjacent dips with 9.7 MHz derives from the hyperfine interaction. Figure 4(b) shows the Rabi oscillation between the $|0_e \quad \downarrow_n\rangle$ and $|-1_e \quad \downarrow_n\rangle$ states in which ($|0_e\rangle$ and $|-1_e\rangle$ represent the electron spin states of $m_s = 0$ and $m_s = -1$, respectively, and $|\downarrow_n\rangle$ represents the nuclear state of $m_I = -1/2$). The blue dots denote the experimental data and they are fitted by a two-cosine exponential decay function (red solid line).

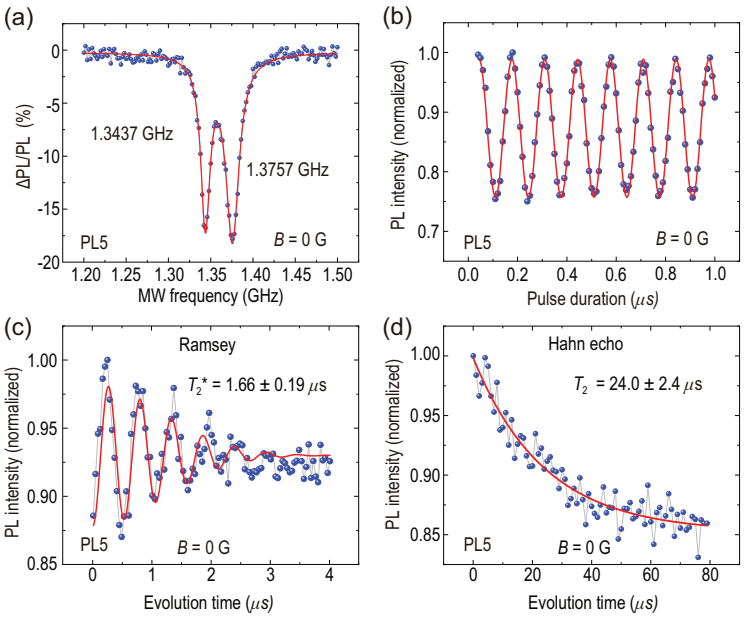

Figure 3. Spin properties of a single PL5 defect spin at room temperature measured in a zero magnetic field. (a) CW-ODMR spectra. The blue dots are the experimental raw data and the red line represents the corresponding Lorentzian-shaped multipeak fitting. (b) Rabi oscillations. The blue dots are the experimental raw data and the red line corresponds to the decaying cosine fittings. (c) Ramsey oscillation. From the fitting, the inhomogeneous spin-dephasing time T_2^* is deduced to be 1.66 ± 0.19 μs. (d) Hahn echo coherence time. From the fitting, the homogeneous spin coherence time T_2 is 24.0 ± 2.4 μs.

THEORETICAL ANALYSIS

The room-temperature readout contrast of the PL5 and PL6 centres in 4H-SiC is strikingly high, which requires a theoretical interpretation. The ODMR contrast of divacancy defects in 4H-SiC can be analysed based on the theory of the ODMR contrast of the NV centre in diamond because they are isovalent centres [10,13]. The so-called *c*-axis divacancy defects, in which the neighbouring carbon and silicon vacancies are situated along the *c* axis of the crystal, possess C_{3v} symmetry similar to the diamond NV centre. The basal divacancy defects exhibit C_{1h} symmetry in 4H-SiC, but it has recently been shown [49] that these configurations can be considered as C_{3v} defects with a spin quantization axis pointing along the connecting line of the vacancies with a perturbation of strain induced by the crystal field. By considering the strain as a relatively small perturbation, one can focus on the C_{3v} symmetry solution as obtained for the diamond NV centre.

The analysis of the ODMR contrasts is based on the known levels and states of the defect (see Fig. 5(a), [50,51] and the references therein) that are labelled according to the C_{3v} point group. The levels are enumerated for the sake of simplicity. The ODMR contrast depends on the relation between the intersystem crossing (ISC) rates (green arrows) and the direct recombination rates (red arrows) as the electron decays from the excited-state manifold (states 4 and 3) to the ground-state manifold (states 1 and 2) via the metastable states (states 6 and 5) and directly, respectively. The strength of the transitions is governed by selection rules and electron-phonon coupling, where the latter results in the vibronic singlet states labelled by a tilde in Fig. 5(a) (see Section 10 of the online supplementary material for details).

The observed ODMR readout contrast depends on a number of factors. To consider the trends, we simplify this complex problem to an expression with parameters that are intrinsic to the defects. In this case, the pulsed off-resonant ODMR readout contrast C can be expressed as

$$C = \frac{\tau_{\pm1} - \tau_0}{\tau_0} = \frac{r_0 - r_{\pm1}}{r_{\pm1}}, \qquad (1)$$

where $r_0 = r_D + r_{36}$ and $r_{\pm1} = r_D + r_{46}$ are the corresponding rates with r_D direct recombination rate, $r_D = r_{42} = r_{31}$, and the respective τ_0 and $\tau_{\pm1}$ are the optical lifetimes (inverse of the rates). The rates r_{36} and r_{46} are the corresponding ISC rates, where r_{36} is extremely weak and can be ignored (see [50] and the references therein). As a consequence, the sign of the ODMR contrast will be negative, as $r_{\pm1} > r_0$ applies in this condition. Equation (1) rests upon four basic assumptions: (i) perfect optical spin polarization of state 1 ($m_s = 0$ ground state) upon long illumination before the readout protocol starts, i.e. perfect initialisation; (ii) photo-excitation of state 1 will preserve the $m_s = 0$ state, i.e. r_{36} is negligible so the reference fluorescence intensity is the fluorescence of the $m_s = 0$ state (state 3); (iii) perfect spin flip upon applying a microwave π pulse in state 1 to rotate it to state 2, so the change in fluorescence intensity is associated with emission from the $m_s = \pm1$ state (state 4); (iv) the change of fluorescence intensity can be perfectly measured, i.e. it is associated with the optical lifetime of the $m_s = \pm1$ state (state 4). We discuss in Section 10 of the online supplementary material how conditions (i)–(iii) are fulfilled from the theoretical point of view. In practice, the measurements are not perfect. In particular, they often fail to satisfy condition (iv). As a consequence, the observed ODMR readout contrasts are weaker than the theoretical limit that is an upper bound for the absolute value of the pulsed ODMR readout contrast. We also emphasize that the deviation from the theoretical limit may strongly vary depending on the applied parameters and technicalities in the actual measurements, even for the same type of divacancy defect. This makes the direct comparison between studies

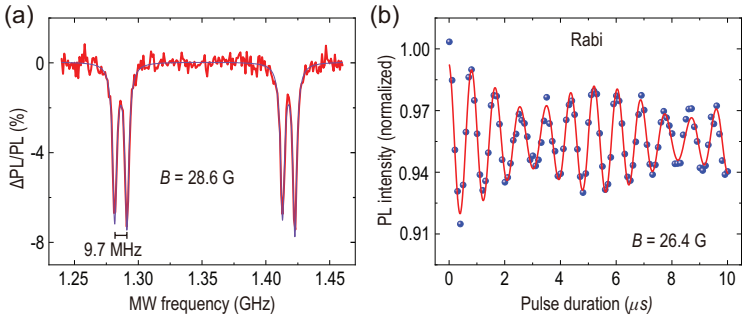

Figure 4. A single PL6 electron spin coupled to a nearby ^{29}Si nuclear spin at room temperature. (a) ODMR spectra in a magnetic field of 28.6 G. (b) Rabi oscillation of the defect spin.

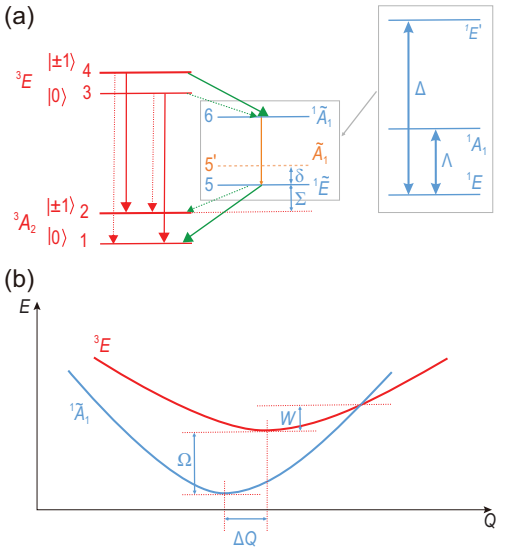

Figure 5. Theoretical model. (a) Defect levels and decay paths in divacancy defects. This simplified diagram is valid at room temperature in the ^3E excited state and at zero strain and magnetic fields. The radiative decays are depicted by the red arrows, whereas the non-radiative processes are shown by the green arrows. Radiative and non-radiative decays compete between the $^1\widetilde{A}_1$ and $^1\widetilde{E}$ singlet states (see the box in the middle of the figure), as depicted by an orange arrow. The very weak transitions are depicted by thin dotted arrows. The tilde represents vibronic states, in which strong electron-phonon coupling mixes the three singlet states, as shown in the box on the right-hand side of the figure. The $\widetilde{A}_1$ state (orange dashed level) is the first excited vibronic state over the $^1\widetilde{E}$ ground state, which plays a role in the temperature dependence of intersystem crossing towards the ground-state manifold. The defect states are enumerated. The corresponding energy gaps are labelled with Greek letters. The energy gaps between the $m_s = \pm 1$ and $m_s = 0$ spin levels are magnified by 6 orders of magnitude for the sake of clarity. (b) Levels crossing between the bright and dark excited states. Schematic energy (E) versus configuration coordinate (Q) diagram for the divacancy defects. At cryogenic temperatures, the energy gap is Ω between the bright ^3E and dark $^1\widetilde{A}_1$ states. The barrier energy for the ^3E state is W in order to reach the crossing point between the two levels.

with different readout parameters or experimental setups ambiguous. Thus, our theory is used to interpret the trends in the observed ODMR contrasts, but is not intended to fully comply with the experimental data.

As an example, we apply this theory to the room-temperature data of single PL6 and PL1 centres; see Fig. S5 of the online supplementary material. By taking the average lifetime data, one obtains −33.6% and −10.0% ODMR readout contrasts, respectively, that are also close to the observed room-temperature ODMR readout contrasts (their average values are −26.4% and −6.6%, respectively). We note that the observed lifetimes show non-negligible uncertainties that affect the results on the derived ODMR readout contrasts. Nevertheless, it may be concluded that the theoretical upper bound limit is indeed manifested. We note that observations on single PL6 centres approach the theoretical limit (31.6%) for one PL6 defect in our study (see Fig. S4B). These results also imply that Equation (1) can be applied to understand the trends in the ODMR contrasts either in terms of various divacancy configurations or temperature dependence of a given divacancy configuration in 4H-SiC. The dissimilarities between the diamond NV centre and SiC divacancies are quantitative and not qualitative.

The ODMR contrast is primarily governed by the rate r_{46}. The rate $r_{46} \propto \lambda_\perp^2 F_A(\Omega)$ depends on the strength of the spin-orbit coupling (perpendicular component, $\lambda_\perp$) and the spectral phonon overlap function F_A with the A_1 phonons that connect the geometries of $|^1\widetilde{A}_1\rangle$ and $|^3E\rangle$ that are originally separated by ΔQ (see Fig. 5(b)). The spin-orbit coupling parameters are of the same order of magnitude for the diamond NV centre and the divacancy defects in SiC (see [10,50] and the references therein); nevertheless, the $\lambda_\perp$ values may differ somewhat for the diamond NV centre and the divacancy configurations, which can contribute to quantitative differences in the final values of r_{46}. On the other hand, the $\lambda_\perp$ values should be very similar for each divacancy configuration because of the common chemical composition. It is likely that the quantitative differences between the r_{46} rates and the corresponding ODMR readout contrasts of the defects dominantly come from the strongly varying F_A values.

The F_A values are sensitive to the low-temperature energy gap between the excited-state triplet and the nearby singlet (Ω in Fig. 5(b); see the discussion in Section 10 of the online supplementary material). The F_A value rapidly increases by closing the gap Ω, which ultimately results in a larger ODMR readout contrast. Since the electronic

states are confined for PL5 and PL6 in the stacking faults (see Section 10 of the online supplementary material), Ω is expected to be smaller for the PL5 and PL6 defects than for the PL1-4 defects, which explains the trends in the low-temperature ODMR contrasts of divacancy configurations in 4H-SiC. However, yielding the room-temperature ODMR contrast requires understanding the temperature dependence of the ODMR contrast, which depends on the temperature dependence of τ_0 and $\tau_{\pm1}$. In a seminal work, it has been found that, for a single diamond NV centre [52], $\tau_{\pm1}$ was almost constant over a wide range of temperatures (300–680 K); however, τ_0 radically decreased for temperatures above 550 K. This can be interpreted such that r_{36}, the non-radiative decay from the triplet $|0\rangle$, was significantly enhanced at elevated temperatures. Authors of the seminal work provided a phenomenological model to explain this phenomenon, the Mott-Seitz formula, which was developed for multiphonon non-radiative processes. Figure 5(b) shows that the bright and dark levels can cross by the dynamic motion of ions. The energy barrier W jumps into this crossing point from the lowest energy of the bright state, which can be reached at an elevated temperature T with the thermal energy k_BT, where k_B is the Boltzmann constant. In this case, the lifetime of state 3, $\tau_0(T)$, can be expressed as

$$\tau_0(T) = \frac{\tau_0(T \approx 0\text{K})}{1 + s\,\exp\left[-W/(k_B T)\right]}, \qquad (2)$$

where s is a dimensionless quantity, interpreted as the fraction of the non-radiative and radiative rates at the crossing point. The energy $W \approx 0.5$ eV is relatively large for the diamond NV centre [51,52]; therefore, the strong temperature dependence on the ODMR readout contrast is only visible from $T \approx 550$ K. However, the energy gaps for divacancy defects in 4H-SiC are much smaller. For instance, $W \approx 0.1$ eV is calculated for the PL1 defect [51]. This result implies that the threshold temperature is much lower for divacancy defects than for the diamond NV centre.

No reported quantitative data is available in the literature about the temperature dependence of the pulsed ODMR readout contrast of divacancy defects in SiC, and our paper focuses on the room-temperature properties. On the other hand, low-temperature off-resonant ODMR contrast data are available on ensemble defects by measuring only the zero-phonon lines [27]. Because of the very different conditions of measurements, the raw CW-ODMR contrast data (e.g. ≈−10% for the PL1 defects) in [27] should be scaled up by a factor (≈1.444) that we estimated from our data by comparing the CW-ODMR contrast and the pulsed ODMR contrast at room temperature (see the details given in Section 10 of the online supplementary material). The estimated pulsed ODMR contrast data with the experimental conditions in our setup and protocol correspond to −14.5%, which reduces to ≈−6.6% at room temperature (see Section 8 of the online supplementary material). Thus, the ODMR contrast of the divacancy defect significantly weakens at elevated temperatures. By using the same procedure with data from [27], the deduced pulsed ODMR contrasts of PL5 and PL6 defects associated with our experimental setup and protocol are ≈−34.7% and ≈−31.8%, respectively. The reduction in the contrasts is not insignificant up to room temperature, but the absolute values of the contrasts still remain relatively high for single PL5 and PL6 defects (≈−26% and ≈−26.4%, respectively, average values in this work), and may approach zero above 650 K [30]. Indeed, our theory can excellently account for the temperature-dependent ODMR readout contrast of PL5 defects observed within a wide temperature range, resulting in $W = 0.076 \pm 0.003$ eV from the fit to data extracted from experiments (see Section 10 of the online supplementary material). The value of W for the PL5 defect is indeed smaller than the calculated $W = 0.1$ eV for the PL1 defect, which is consistent with our quantum confinement theory on the defect levels of divacancy defects in the stacking fault (see Section 10 of the online supplementary material).

CONCLUSION

In conclusion, we presented a scalable method for the creation of single divacancy spin defects in 4H-SiC using carbon ion implantation and combining electron beam lithography and post-annealing techniques. We characterized the spin properties and demonstrated the coherent manipulation of individual spin defects, including PL1, PL5, PL6 and PL7 defects, at room temperature. Surprisingly, single PL6 spin defects have some outstanding properties compared with several previously reported spin defects in SiC [9–11,14,19]. The saturated count rate of a single PL6 centre is up to 150 kcps, and its CW-ODMR and Rabi oscillation contrasts can reach as high as −23% and −30%, respectively, which are comparable with those of single-NV colour centres in diamond. By analysing the defect levels and decay paths, we provided a theoretical model to explain the observed high ODMR contrast, which can also be applied to understand the trends in the ODMR contrasts of different divacancy configuration and their temperature-dependent properties in 4H-SiC.

The divacancy qubits reported in this work have near-infrared excitation and emission in a wavelength region that is the most transparent to living cells; this is in stark contrast to the NV centres in diamond that require green illumination for efficient photo-excitation, causing high auto-fluorescence of living cells. Besides, the longer laser wavelength required for ODMR measurements of colour centres in SiC is advantageous in biological applications, compared with the NV centres in diamond, regarding the photo-toxicity. This makes divacancy colour centres highly prospective for preclinical and human diagnostic applications and therapy as similar divacancy defects have been engineered into water soluble SiC nanocrystals [53]. Integrating spin defects with a high readout contrast and a high photon count rate into high-performance SiC electron devices and recently developed integrated optical chips based on SiC [54] may also provide considerable opportunities for the next generation of hybrid quantum devices.

METHODS

Sample preparation

In our work, a 12.5-μm-thick epitaxial layer of single-crystal 4H-SiC with a nitrogen doping density of 5×10^{15} cm^{-3} grown on a 4° off-axis 4H-SiC substrate was used [22,35]. A layer of positive electron beam photoresist PMMA A4 with a thickness of approximately 200 nm was spin coated onto the surface of the SiC sample. Through electron beam lithography (EBL, JEOL, JBX 6300FS), an array of apertures with a pitch of 2 μm and a diameter of 50 ± 10 nm was fabricated on the surface of the sample as a mask. Then, the sample was implanted with 30-keV C^+ ions at a dose of 1.02×10^{12} cm^{-2}. There were approximately 20 implanted carbon ions per aperture in the sample. The mask was then removed using an ultrasonic bath of acetone solution. The sample was annealed in a tube furnace at 900 °C for 30 minutes in a vacuum environment of approximately 1×10^{-4} Pa. Finally, the sample was cleaned in a 3 : 1 mixture of concentrated sulfuric acid and hydrogen peroxide and heated to 95 °C for 5 hours, which dramatically reduced the background fluorescence. Single-spin defects could then be optically addressed.

Optical measurements

A home-built scanning confocal microscope with an infrared oil objective with an NA of 1.3 (Nikon, CFI Plan Fluor 100X Oil) was used in our experiments. In all of the optical measurements, a 920-nm CW laser, filtered by a shortpass filter (Thorlabs, FESH950), was used to excite those colour centres. A dichroic beamsplitter (Semrock, Di02-R980-25×36) was then used to separate the laser and fluorescence signals. For various measurements at room temperature, the SiC samples were mounted on a closed cycle three-axis piezoelectric stage (PI, E-727.3SD). The fluorescence signals filtered by a 1000-nm longpass filter (Thorlabs, FELH1000) were coupled to a single-mode fibre and then guided to a superconducting nanowire single-photon detector (SNSPD, Scontel & Photon Technology) with an approximately 80% quantum efficiency. The number of photons was recorded by a counter (NI, USB-6341). For the HBT measurements, the fluorescence signals were divided by a fibre beam splitter and detected using a two-channel SNSPD. The coincidence correlation with variable delay time t was measured using a time-to-digital converter (IDQ, ID800-TDC).

Spin coherent manipulation

The same home-built scanning confocal microscope was used to polarize and readout the optical signals depending on the spin states of the isolated defects. For the ODMR, Rabi, Ramsey and spin echo measurements, the microwave sequences were generated using a synthesized signal generator (Mini-Circuits, SSG-6000 RC) and then gated by a switch (Mini-Circuits, ZASWA-2-50DR+). After amplification (Mini-Circuits, ZHL-25W-272+), the microwave signals were fed to a 50-μm-wide copper wire above the surface of the 4H-SiC sample. The exciting 920-nm CW laser was modulated using an acousto-optic modulator. The timing sequence of the electrical signals for manipulating and synchronizing the laser, microwave and counter was generated using a pulse generator (SpinCore, PBESR-PRO500).

SUPPLEMENTARY DATA

Supplementary data are available at *NSR* online.

ACKNOWLEDGEMENTS

We thank Gang-Qin Liu from Institute of Physics, Chinese Academy of Sciences for his helpful discussion. This work was partially carried out at the USTC Centre for Micro- and Nanoscale Research and Fabrication.

FUNDING

This work was supported by the National Key Research and Development Program of China (2016YFA0302700), the National

Natural Science Foundation of China (U19A2075, 61725504, 61905233, 11774335, 11821404 and 11975221), the Key Research Program of Frontier Sciences, CAS (QYZDY-SSW-SLH003), the Science Foundation of the CAS (ZDRW-XH-2019-1), the Anhui Initiative in Quantum Information Technologies (AHY060300 and AHY020100), the Fundamental Research Funds for the Central Universities (WK2030380017 and WK2470000026), the National Postdoctoral Program for Innovative Talents (BX20200326). A.G. acknowledges support from the National Research, Development and Innovation Office of Hungary (NKFIH) for Quantum Technology Program (2017-1.2.1-NKP-2017-00001), the National Excellence Program (KKP129866), the EU QuantERA Nanospin Project (NKFIH Grant No. NN127902) as well as the Quantum Information National Laboratory sponsored by the Ministry of Innovation and Technology of Hungary.

AUTHOR CONTRIBUTIONS

Q.L., J.-F.W. and J.-S.X. designed the experiments. Q.L. and H.L. prepared the PMMA mask with the support of G.-P.G. L.-P.G. and X.Z. performed the ion implantation experiments. Q.L. carried out the experiments assisted by J.-F.W., F.-F.Y., J.-Y.Z., H.-F.W., Z.-H.L., Z.-Q.W., K.S., J.-S.T. and J.-S.X. A.G. provided the theoretical support. J.-S.X., C.-F.L. and G.-C.G. supervised the project. Q.L., J.-S.X. and A.G. wrote the paper with input from other authors. All authors discussed the experimental procedures and results.

Conflict of interest statement. None declared.

REFERENCES

1. Atatüre M, Englund D and Vamivakas N *et al.* Material platforms for spin-based photonic quantum technologies. *Nat Rev Mater* 2018; **3**: 38–51.
2. Awschalom DD, Hanson R and Wrachtrup J *et al.* Quantum technologies with optically interfaced solid-state spins. *Nat Photon* 2018; **12**: 516–27.
3. Castelletto S and Boretti A. Silicon carbide color centers for quantum applications. *J Phys Photonics* 2020; **2**: 022001.
4. Son NT, Anderson CP and Bourassa A *et al.* Developing silicon carbide for quantum spintronics. *Appl Phys Lett* 2020; **116**: 190501.
5. Lohrmann A, Iwamoto N and Bodrog Z *et al.* Single-photon emitting diode in silicon carbide. *Nat Commun* 2015; **6**: 7783.
6. Khramtsov IA, Vyshnevyy AA and Fedyanin DY. Enhancing the brightness of electrically driven single-photon sources using colour centres in silicon carbide. *npj Quantum Inf* 2018; **4**: 15.
7. Sato SI, Honda T and Makino T *et al.* Room temperature electrical control of single photon sources at 4H-SiC surface. *ACS Photonics* 2018; **5**: 3159–65.
8. Widmann M, Niethammer M and Makino T *et al.* Bright single photon sources in lateral silicon carbide light emitting diodes. *Appl Phys Lett* 2018; **112**: 231103.
9. Christle DJ, Falk AL and Andrich P *et al.* Isolated electron spins in silicon carbide with millisecond coherence times. *Nat Mater* 2015; **14**: 160–3.
10. Christle DJ, Klimov PV and de las Casas CF *et al.* Isolated spin qubits in SiC with a high-fidelity infrared spin-to-photon interface. *Phys Rev X* 2017; **7**: 021046.
11. Widmann M, Lee SY and Rendler T *et al.* Coherent control of single spins in silicon carbide at room temperature. *Nat Mater* 2015; **14**: 164–8.
12. Miao KC, Blanton JP and Anderson CP *et al.* Universal coherence protection in a solid-state spin qubit. *Science* 2020; **369**: 1493–7.
13. Gali A. Time-dependent density functional study on the excitation spectrum of point defects in semiconductors. *Phys Status Solidi B* 2011; **248**: 1337–46.
14. Koehl WF, Buckley BB and Heremans FJ *et al.* Room temperature coherent control of defect spin qubits in silicon carbide. *Nature* 2011; **479**: 84–7.
15. Anderson CP, Bourassa A and Miao KC *et al.* Electrical and optical control of single spins integrated in scalable semiconductor devices. *Science* 2019; **366**: 1225–30.
16. Janzén E, Gali A and Carlsson P *et al.* The silicon vacancy in SiC. *Physica B* 2009; **404**: 4354–8.
17. Fuchs F, Stender B and Trupke M *et al.* Engineering near-infrared single-photon emitters with optically active spins in ultrapure silicon carbide. *Nat Commun* 2015; **6**: 7578.
18. Nagy R, Niethammer M and Widmann M *et al.* High-fidelity spin and optical control of single silicon-vacancy centres in silicon carbide. *Nat Commun* 2019; **10**: 1954.
19. Soltamov VA, Kasper C and Poshakinskiy AV *et al.* Excitation and coherent control of spin qudit modes in silicon carbide at room temperature. *Nat Commun* 2019; **10**: 1678.
20. Zargaleh SA, Eble B and Hameau S *et al.* Evidence for near-infrared photoluminescence of nitrogen vacancy centers in 4H-SiC. *Phys Rev B* 2016; **94**: 060102.
21. Csóré A, von Bardeleben HJ and Cantin JL *et al.* Characterization and formation of NV centers in 3*C*, 4*H*, and 6*H* SiC: an *ab initio* study. *Phys Rev B* 2017; **96**: 085204.
22. Wang JF, Yan FF and Li Q *et al.* Coherent control of nitrogen-vacancy center spins in silicon carbide at room temperature. *Phys Rev Lett* 2020; **124**: 223601.
23. Mu Z, Zargaleh SA and von Bardeleben HJ *et al.* Coherent manipulation with resonant excitation and single emitter creation of nitrogen vacancy centers in 4H silicon carbide. *Nano Lett* 2020; **20**: 6142–7.
24. Klimov PV, Falk AL and Christle DJ *et al.* Quantum entanglement at ambient conditions in a macroscopic solid-state spin ensemble. *Sci Adv* 2015; **1**: e1501015.
25. Falk AL, Buckley BB and Calusine G *et al.* Polytype control of spin qubits in silicon carbide. *Nat Commun* 2013; **4**: 1819.
26. Wolfowicz G, Whiteley SJ and Awschalom DD. Electrometry by optical charge conversion of deep defects in 4H-SiC. *Proc Natl Acad Sci USA* 2018; **115**: 7879–83.
27. Falk AL, Klimov PV and Buckley BB *et al.* Electrically and mechanically tunable electron spins in silicon carbide color centers. *Phys Rev Lett* 2014; **112**: 187601.
28. Whiteley SJ, Heremans FJ and Wolfowicz G *et al.* Correlating dynamic strain and photoluminescence of solid-state defects with stroboscopic X-ray diffraction microscopy. *Nat Commun* 2019; **10**: 3386.

29. Zhou Y, Wang J and Zhang X *et al.* Self-protected thermometry with infrared photons and defect spins in silicon carbide. *Phys Rev Appl* 2017; **8**: 044015.
30. Yan FF, Wang JF and Li Q *et al.* Coherent control of defect spins in silicon carbide above 550 K. *Phys Rev Appl* 2018; **10**: 044042.
31. Klimov PV, Falk AL and Buckley BB *et al.* Electrically driven spin resonance in silicon carbide color centers. *Phys Rev Lett* 2014; **112**: 087601.
32. Whiteley SJ, Wolfowicz G and Anderson CP *et al.* Spin-phonon interactions in silicon carbide addressed by Gaussian acoustics. *Nat Phys* 2019; **15**: 490–5.
33. Ivády V, Davidsson J and Delegan N *et al.* Stabilization of point-defect spin qubits by quantum wells. *Nat Commun* 2019; **10**: 5607.
34. Radulaski M, Widmann M and Niethammer M *et al.* Scalable quantum photonics with single color centers in silicon carbide. *Nano Lett* 2017; **17**: 1782–6.
35. Wang JF, Li Q and Yan FF *et al.* On-demand generation of single silicon vacancy defects in silicon carbide. *ACS Photonics* 2019; **6**: 1736–43.
36. Gruber A, Dräbenstedt A and Tietz C *et al.* Scanning confocal optical microscopy and magnetic resonance on single defect centers. *Science* 1997; **276**: 2012–4.
37. Dréau A, Lesik M and Rondin L *et al.* Avoiding power broadening in optically detected magnetic resonance of single NV defects for enhanced DC magnetic field sensitivity. *Phys Rev B* 2011; **84**: 195204.
38. Wolfowicz G, Anderson CP and Yeats AL *et al.* Optical charge state control of spin defects in 4H-SiC. *Nat Commun* 2017; **8**: 1876.
39. Castelletto S, Johnson BC and Ivády V *et al.* A silicon carbide room-temperature single-photon source. *Nat Mater* 2014; **13**: 151–6.
40. Wang J, Zhou Y and Wang Z *et al.* Bright room temperature single photon source at telecom range in cubic silicon carbide. *Nat Commun* 2018; **9**: 4106.
41. Rondin L, Tetienne JP and Hingant T *et al.* Magnetometry with nitrogen-vacancy defects in diamond. *Rep Prog Phys* 2014; **77**: 056503.
42. de Lange G, Wang ZH and Ristè D *et al.* Universal dynamical decoupling of a single solid-state spin from a spin bath. *Science* 2010; **330**: 60–3.
43. Ryan CA, Hodges JS and Cory DG. Robust decoupling techniques to extend quantum coherence in diamond. *Phys Rev Lett* 2010; **105**: 200402.
44. Bourassa A, Anderson CP and Miao KC *et al.* Entanglement and control of single nuclear spins in isotopically engineered silicon carbide. *Nat Mater* 2020; **19**: 1319–25.
45. Morioka N, Babin C and Nagy R *et al.* Spin-controlled generation of indistinguishable and distinguishable photons from silicon vacancy centres in silicon carbide. *Nat Commun* 2020; **11**: 2516.
46. Kennedy TA, Colton JS and Butler JE. Long coherence times at 300 K for nitrogen-vacancy center spins in diamond grown by chemical vapor deposition. *Appl Phys Lett* 2003; **83**: 4190–2.
47. Yamamoto T, Umeda T and Watanabe K *et al.* Extending spin coherence times of diamond qubits by high-temperature annealing. *Phys Rev B* 2013; **88**: 075206.
48. Falk AL, Klimov PV and Ivády V *et al.* Optical polarization of nuclear spins in silicon carbide. *Phys Rev Lett* 2015; **114**: 47603.
49. Miao KC, Bourassa A and Anderson CP *et al.* Electrically driven optical interferometry with spins in silicon carbide. *Sci Adv* 2019; **5**: eaay0527.
50. Gali Á. Ab initio theory of the nitrogen-vacancy center in diamond. *Nanophotonics* 2019; **8**: 1907–43.
51. Bockstedte M, Schütz F and Garratt T *et al.* Ab initio description of highly correlated states in defects for realizing quantum bits. *npj Quantum Mater* 2018; **3**: 31.
52. Toyli DM, Christle DJ and Alkauskas A *et al.* Measurement and control of single nitrogen-vacancy center spins above 600 K. *Phys Rev X* 2012; **2**: 031001.
53. Beke D, Valenta J and Károlyházy G *et al.* Room-temperature defect qubits in ultrasmall nanocrystals. *Phys Chem Lett* 2020; **11**: 1675–81.
54. Lukin DM, Dory C and Guidry MA *et al.* 4H-silicon-carbide-on-insulator for integrated quantum and nonlinear photonics. *Nat Photon* 2020; **14**: 330–4.